Laser differential confocal radius measurement

Weiqian Zhao,* Ruoduan Sun, Lirong Qiu, and Dingguo Sha

Key Laboratory of Photoelectronic Imaging Technology and System (Ministry of Education of China),
Opto-Electronic College, Beijing Institute of Technology, Beijing 100081, China
*zwq669@126.com

Abstract: A new laser differential confocal radius measurement (DCRM) is proposed for high precision measurement of radius. Based on the property of an axial intensity curve that the absolute zero precisely corresponds to the focus of the objective in a differential confocal system (DCS), DCRM uses the zero point of the DCS axial intensity curve to precisely identify the cat's-eye and confocal positions of the test lens, and measures the accurate distance between the two positions to achieve the high-precision measurement of radius of curvature (ROC). In comparison with the existing measurement methods, DCRM proposed has a high measurement precision, a strong environmental anti-interference capability and a low cost. The theoretical analyses and preliminary experimental results indicate that DCRM has a relative measurement error of better than 5ppm.

References and links

1. P. Becker, H. Friedrich, and K. Fujii, "WGiardini, G Mana, A Picard, H-J Pohl, H Riemann and S Valkiers, "The Avogadro constant determination via enriched silicon-28," Meas. Sci. Technol. **20**, 1–20 (2009).
2. D. Malacara, "Optical Shop Testing, 2nd edition," (Wiley-Interscience, 1992), Chap17.
3. L. A. Selberg, "Radius measurement by interferometry," Opt. Eng. **31**(9), 1961–1966 (1992).
4. Y. Xiang, "Focus retrocollimated interferometry for long-radius-of-curvature measurement," Appl. Opt. **40**(34), 6210–6214 (2001).
5. Y. Pi, and P. J. Reardon, "Determining parent radius and conic of an off-axis segment interferometrically with a spherical reference wave," Opt. Lett. **32**(9), 1063–1065 (2007).
6. U. Griesmann, J. Soons, Q. Wang, and D. DeBra, "Measuring form and radius of sphere with interferometry," Ann. CIRP **53**(1), 451–454 (2004).
7. Q. Hao, Q. Zhu, and Y. Hu, "Random phase-shifting interferometry without accurately controlling or calibrating the phase shifts," Opt. Lett. **34**(8), 1288–1290 (2009).
8. T. L. Schmitz, C. J. Evans, A. D. Davies and W. T. Estler, "Displacement Uncertainty in Interferometric Radius Measurements," CIRP Annals - Manufacturing Technology, **51**, 451–454 (2002).
9. T. L. Schmitz, A. D. Davies, and C. J. Evans, "Uncertainties in interferometric measurements of radius-of-curvature," Proc. SPIE **4451**, 432–447 (2001).
10. W. Zhao, J. Tan, and L. Qiu, "Bipolar absolute differential confocal approach to higher spatial resolution," Opt. Express **12**(21), 5013–5021 (2004).
11. W. Zhao, J. Tan, L. Qiu, and P. Jin, "SABCMS, A New Approach to Higher Lateral Resolution of Laser Probe Measurement," Sens. Actuators A Phys. **120**(1), 17–25 (2005).
12. L. Liu, X. Deng, and G. Wang, "Phase-only optical pupil filter for improving axial resolution in confocal microscopy," Acta Phys. Sin. **50**, 48–51 (2001).
13. M. Born, and E. Wolf, Principles of Optics (Cambridge University Press, 1999), Chap. 9.
14. A. Davies, and T. L. Schmitz, "Correcting for stage error motions in radius measurements," Appl. Opt. **44**(28), 5884–5893 (2005).
15. T. L. Schmitz, N. Gardner, M. Vaughn, K. Medicus, and A. Davies, "Improving optical bench radius measurements using stage error motion data," Appl. Opt. **47**(36), 6692–6700 (2008).

---

1. Introduction

Sphere component is widely used in precise optical systems as the most essential optical component, such as violet lithography, astronomical telescope and laser fusion program. The radius of curvature (ROC) is one of the most basic and important parameters in the sphere surface measurement, and the high precision ROC measurement is still a difficulty [1]. At present, the main methods used for ROC measurement include spherometer, Foucault test,

traveling microscope, focus retrocollimated interferometry, autocollimation, simple fiber-optic autocollimation method and figure measuring interferometer(FMI), and so on [2–6]. In the aforementioned methods, FMI is the most well-known method used for the ROC accurate measurement, which uses the interference fringe to identify the cat's eye and confocal positions, and measures the accurate distance between the two positions to obtain the ROC. The common FMI uses PZT for phase-shifting, and has disadvantages as below. 1) It is difficult for the measurement beam to converge to a point due to the diffraction and the focal-depth restricts the accuracy of identification at the cat's-eye and confocal positions. 2) The environmental vibration and airflow have an adverse effect on the stability of interference fringe at the cat's-eye and confocal positions [7,9]. To improve the anti-interference capability, the instantaneous phase shifting interferometry was developed, but it is expensive and complex.

And therefore, a low-cost, compact laser differential confocal radius measurement (DCRM) is proposed, which has a high accuracy of the identifications at cat's-eye and confocal points and a stronger anti-interference capability by using the differential confocal intensity detection [10,11]. In addition, DCRM is easy to be combined with a pupil filter and it can shorten the focal-depth to further improve the accuracy of the identifications at the cat's-eye and confocal positions [12].

2. Measurement principle

2.1 DCRM principle

Based on the property that the zero point of the axial intensity curve corresponds to the focus of the objective in a differential confocal system (DCS) established by ourselves [10,11], DCRM as shown in Fig. 1 uses the null points O_A and O_B of DCS axial intensity curves I_A and I_B to make precise identifications at the cat's-eye position A and confocal position B of the test sphere, and measures the distance between the two null positions to achieve the ROC accurate measurement.
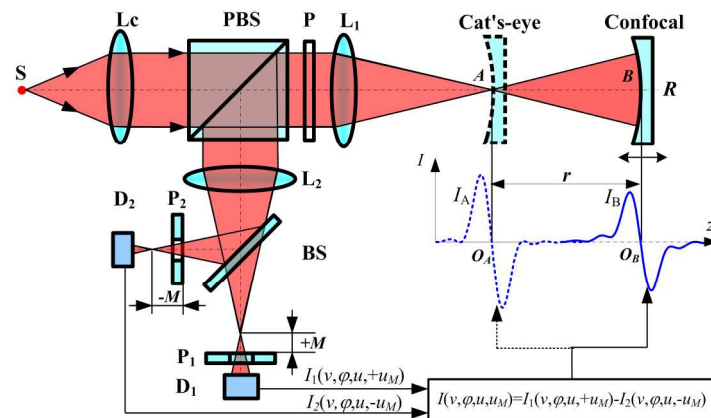

Fig. 1. DCRM principle.

As shown in Fig. 1, L_C is collimating lens, PBS is polarized beam splitter, P is $\lambda/4$, L_1 is standard focusing lens, L_2 is collecting lens, BS is beam splitter, S is point light source, D_1 and D_2 are detectors, P_1 and P_2 are pinholes, R is test lens, M is the offset of pinhole from the focus of L_2.

When the test lens R is moved near the cat's-eye position A along the optical axis, the measurement beam is reflected along the backtracking by the lens R and then reflected on the collecting lens L_2 and BS by PBS, and the two measurement beam split by BS are received by detectors D_1 and D_2, respectively. Near the cat's-eye position A, the overlap area of the measurement beam and the test surface is so small that the effect of the figure error on the DCS intensity curve is negligible. Then the signal $I_A(v,\varphi,u,u_M)$ obtained through the

differential subtraction of $I_{A1}(v,\varphi,u, + u_M)$ and $I_{A2}(v,\varphi,u,-u_M)$ received by the detectors D_1 and D_2 is [10,11]

$$I_A(v,\varphi,u,u_M) = I_{A1}(v,\varphi,u,+u_M) - I_{A2}(v,\varphi,u,-u_M)$$

$$= \left| \frac{1}{\pi} \int_0^{2\pi} \int_0^1 p_C(\rho,\theta) \cdot p_1(\rho,\theta) \cdot p_1(\rho,\pi+\theta) \cdot p_2(\rho,\pi+\theta) \cdot e^{j\rho^2(2u+u_M)/2} \cdot e^{-j\rho v\cos(\theta-\varphi)} \rho d\rho d\theta \right|^2 -$$

$$\left| \frac{1}{\pi} \int_0^{2\pi} \int_0^1 p_C(\rho,\theta) \cdot p_1(\rho,\theta) \cdot p_1(\rho,\pi+\theta) \cdot p_2(\rho,\pi+\theta) \cdot e^{j\rho^2(2u-u_M)/2} \cdot e^{-j\rho v\cos(\theta-\varphi)} \rho d\rho d\theta \right|^2$$

(1)

where

$$\begin{cases} u = \dfrac{\pi}{2\lambda}\left(\dfrac{D}{f'}\right)^2 z \\[2mm] v = \dfrac{\pi}{2\lambda}\left(\dfrac{D}{f'}\right) r_0 \end{cases}$$

(2)

where ρ is the radial normalized radius of a pupil, θ is the angle of variable ρ in the polar coordinate, u is the axial normalized optical coordinate, v is the lateral normalized optical coordinate, φ is the angle of variable v in the polar coordinate, z is the axial displacement of the object, r_0 is the radial coordinate of the objective, D/f' is the relative aperture of DCS objective L_1, $p_1(\rho,\theta)$ is the pupil function of L_1, $p_2(\rho,\theta)$ is the pupil function of L_2 and $p_C(\rho,\theta)$ is the pupil function of L_C.

When L_1 and L_2 are the same in apertures, $p_C(\rho,\theta) = 1$, $p_1(\rho,\theta) = 1$, $p_2(\rho,\theta) = 1$, $I_A(0,0,u,u_M)$ obtained from Eq. (1) is:

$$I_A(0,0,u,u_M) = \left| 2\int_0^1 e^{j\rho^2(2u+u_M)/2} \rho d\rho \right|^2 - \left| 2\int_0^1 e^{j\rho^2(2u-u_M)/2} \rho d\rho \right|^2$$

$$= \left[\frac{\sin\left[(2u+u_M)/4\right]}{(2u+u_M)/4} \right]^2 - \left[\frac{\sin\left[(2u-u_M)/4\right]}{(2u-u_M)/4} \right]^2 .$$

(3)

And as shown in Fig. 1, the zero point O_A of intensity curve $I_A(0,0,u,u_M)$ precisely corresponds to the cat's-eye position A of the test lens.

Near the confocal position B, the overlap area of the measurement beam and the test surface is so great that the effect of the figure error $\Phi(\rho,\theta)$ on the DCS intensity curve cannot be ignored, which introduced the wave-front error of $2\Phi(\rho,\theta)$ in the measurement. When the test lens R is moved near the confocal position B along the optical axis, the signal $I_B(v,\varphi,u,u_M,\Phi)$ obtained through the differential subtraction of $I_{B1}(v,\varphi,u, + u_M,\Phi)$ and $I_{B2}(v,\varphi,u,-u_M,\Phi)$ received by detectors D_1 and D_2 is [10,11]

$$I_B(v,\varphi,u,u_M,\Phi) = I_{B1}(v,\varphi,u,+u_M,\Phi) - I_{B2}(v,\varphi,u,-u_M,\Phi)$$

$$= \left| \frac{1}{\pi} \int_0^{2\pi} \int_0^1 p_C(\rho,\theta) \cdot p_1^2(\rho,\theta) \cdot p_2(\rho,\theta) \cdot e^{j\rho^2(2u+u_M)/2} \cdot e^{-j2k\Phi(\rho,\theta)} \cdot e^{-j\rho v\cos(\theta-\varphi)} \rho d\rho d\theta \right|^2 -$$

$$\left| \frac{1}{\pi} \int_0^{2\pi} \int_0^1 p_C(\rho,\theta) \cdot p_1^2(\rho,\theta) \cdot p_2(\rho,\theta) \cdot e^{j\rho^2(2u-u_M)/2} \cdot e^{-j2k\Phi(\rho,\theta)} \cdot e^{-j\rho v\cos(\theta-\varphi)} \rho d\rho d\theta \right|^2$$

(4)

And as shown in Fig. 1, the zero point O_B of intensity curve $I_B(0,0,u,u_M)$ precisely corresponds to the confocal position B of the test lens.

2.2 Effect of $\Phi(\rho,\theta)$ on the accuracy of identification at confocal position B

As shown in Fig. 2, figure error $\Phi(\rho,\theta)$ can make the average radius r_{avg} (best-fit sphere) of the test lens R deviate from r and the DCRM intensity response curve change in shape under the high precision ROC measurement.
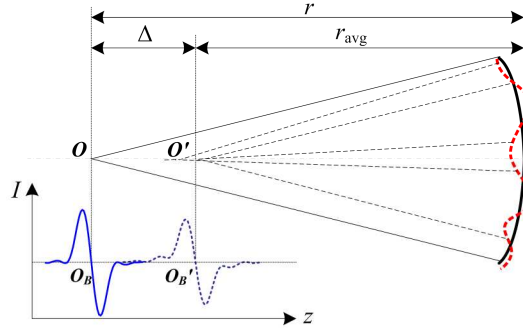

Fig. 2. Effect of $\Phi(\rho,\theta)$ on identification precision at confocal position B.

When several primary aberrations with the distinct effect on ROC measurement are considered, the figure error $\Phi(\rho,\theta)$ is [13]

$$\Phi(\rho,\theta) \approx A_{040}\rho^4 + A_{022}\rho^2\cos^2\theta + A_{031}\rho^3\cos\theta + A_{120}\rho^2 + A_{111}\rho\cos\theta \qquad (5)$$

where A_{040} is the primary spherical aberration coefficient, A_{022} is the astigmatism coefficient, A_{031} is the coma coefficient, A_{120} is the curvature of field coefficient and A_{111} is the distortion coefficient.

$A_{040}\rho^4$ and $A_{022}\rho^2\cos^2\theta$ can incur the axial offset of best-fit sphere center of curvature according to the Displacement Theorem [13], and the normalized axial offset Δ is

$$\Delta \approx \frac{2\pi}{\lambda}(2A_{040} + A_{022}) \qquad (6)$$

Δ is the offset of r_{avg} from r caused by $\Phi(\rho,\theta)$.

Let $p_C(\rho,\theta) = 1$, $p_1(\rho,\theta) = 1$ and $p_2(\rho,\theta) = 1$, $A_{040}\rho^4$ and $A_{022}\rho^2\cos^2\theta$ are substituted for Eq. (4), respectively, then

$$I_{BA_{040}}(v,\varphi,u,u_M,\Phi) = \left| \frac{1}{\pi}\int_0^{2\pi}\int_0^1 e^{j\rho^2(2u+u_M)/2} \cdot e^{-j2kA_{040}\rho^4} \cdot e^{-j\rho v\cos(\theta-\varphi)}\rho d\rho d\theta \right|^2 - $$
$$\left| \frac{1}{\pi}\int_0^{2\pi}\int_0^1 e^{j\rho^2(2u-u_M)/2} \cdot e^{-j2kA_{040}\rho^4} \cdot e^{-j\rho v\cos(\theta-\varphi)}\rho d\rho d\theta \right|^2 \qquad (7)$$

$$I_{BA_{022}}(v,\varphi,u,u_M,\Phi) = \left| \frac{1}{\pi}\int_0^{2\pi}\int_0^1 e^{j\rho^2(2u+u_M)/2} \cdot e^{-j2kA_{022}\rho^2\cos^2\theta} \cdot e^{-j\rho v\cos(\theta-\varphi)}\rho d\rho d\theta \right|^2 - $$
$$\left| \frac{1}{\pi}\int_0^{2\pi}\int_0^1 e^{j\rho^2(2u-u_M)/2} \cdot e^{-j2kA_{022}\rho^2\cos^2\theta} \cdot e^{-j\rho v\cos(\theta-\varphi)}\rho d\rho d\theta \right|^2 \qquad (8)$$

From Eq. (7) and (8), the intensity response curves $I_{BA040}(0,0,u,u_M,\Phi)$ and $I_{BA022}(0,0,u,u_M,\Phi)$ considering the primary spherical aberration $A_{040}\rho^4$ and primary astigmatism $A_{022}\rho^2\cos^2\theta$ at confocal positions B are shown in Fig. 3a) and Fig. 3b), respectively.
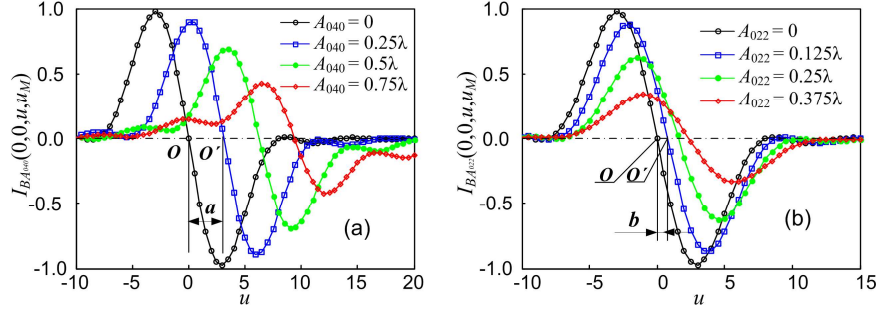
Fig. 3. Effect of figure error $\Phi(\rho,\theta)$ on identification precision at confocal position B. a) Spherical aberration $A_{040}\rho^4$ b) Astigmatism $A_{022}\rho^2\cos^2\theta$.

It can be seen from Fig. 3 that the relation between axial offset Δ of best-fit sphere centre of curvature O' and the axial offsets of zero points of DCRM curves I_{BA040} and I_{BA022} is almost coincide with Eq. (6), i.e., the ROC obtained by DCRM is coincident with r_{avg}. And therefore, $\Phi(\rho,\theta)$ has a very small effect on the accuracy of the measurement by DCRM.

2.3 Effect of $\Phi(\rho,\theta)$ on identification sensitivity

Sensitivity $S_B(0,0,0,C,\Phi)$ at zero point O_B can be obtained by differentiating Eq. (4) on u and is

$$S_B(0,0,0,C,\Phi) = \frac{\partial I_B(v,\varphi,u,u_M,\Phi)}{\partial u}\bigg|_{\varphi=0,u=0,v=0,u_M=C} . \quad (9)$$

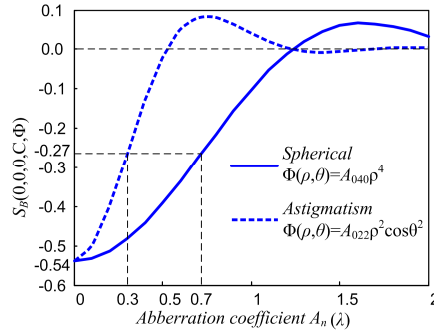Sensitivity curve $S_B(0,0,0,C,\Phi)$ obtained from Eq. (9) is shown in Fig. 4.

Fig. 4. Effect of figure error $\Phi(\rho,\theta)$ on sensitivity curves.

It can be seen from Fig. 4 that DCRM sensitivity $S_B(0,0,0,C,\Phi)$ decreases as the aberration coefficient A_n increases and $|S_B(0,0,0,C,\Phi)|>0.27$ which is half of that without aberrations when $A_{040}<0.7\lambda$ and $A_{022}<0.3\lambda$. And so, the accuracy of identification by DCRM entirely satisfies measurement requirements of the accuracy for the ROC measurement.

It is therefore that the accuracy of the measurement by DCRM is high and the effect of aberrations on DCRM is small as the surface figure precision of sphere measured is high when it is used for the high-precision radius measurement.

3. DCRM system using virtual pinhole for tracking

As shown in Fig. 1, DCRM requires that the pinhole center is coincident with the optical axis and the center of the Airy disk coming from the collecting lens L_2 exactly passes through the pinhole. In the measurement procedure, it is difficult to make the optical axes in coincidence between the test lens R and DCRM, and the axes offset between them results in the lateral offset of the focus of collecting lens L_2. The lateral offset of the pinhole from the focus has an effect on DRCM intensity curve $I(z)$ result in an effect on the sensitivity and precision of the

identification. And the alignment error arising from the measurement line and datum line incur Abbe errors in DCRM.

In order to reduce the assembly difficulty of the test lens and measurement error caused by the assembly of the lens, a virtual pinhole (VPH) using CCD detection as shown in Fig. 5 is substituted for a conventional physical pinhole (PH).
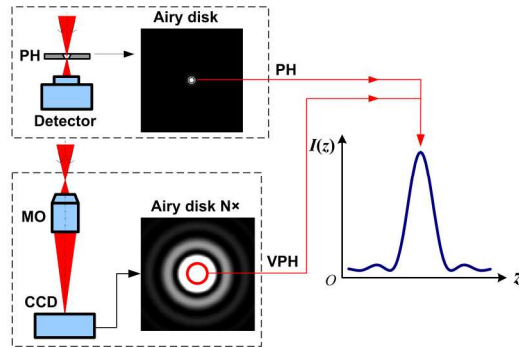

Fig. 5. Virtual pinhole detection principle.

The Airy disk on the L_2 focal plane is magnified and imaged on the CCD detector by microscope objective MO, and the centre coordinates $P(x,y)$ of the Airy disk is obtained using image $g(m,n)$ from CCD based on Eq. (10).

$$\begin{cases} x = \left(\sum_{m,n} m \cdot g(m,n) \right) \Big/ \sum_{m,n} g(m,n) \\ y = \left(\sum_{m,n} n \cdot g(m,n) \right) \Big/ \sum_{m,n} g(m,n) \end{cases} \tag{10}$$

where m and n the pixel coordinate of the image.

And then, the VPH with a given radius r_{VPH} is centered at point $P(x, y)$, the grey summation of pixels within the circle of VPH is calculated, and the circle is equivalent to the physical pinhole of a confocal microscopy system and its size and shape can be adjusted by the software.

DCRM system (DCRMS) using CCD tracking detection by VPH is established as shown in Fig. 6 based on the measurement principle shown in Fig. 1 and VPH technique.
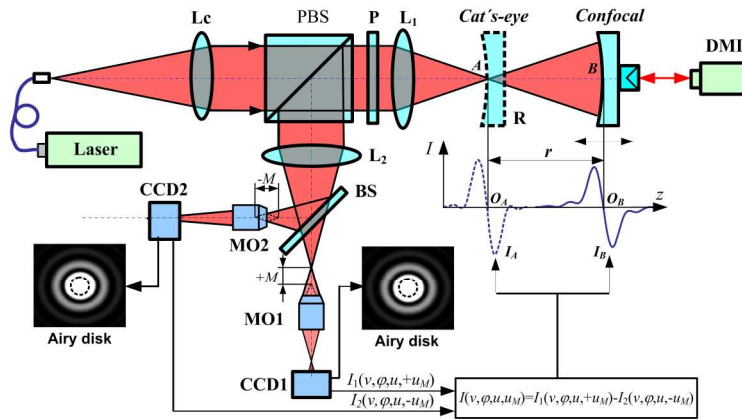

Fig. 6. DCRMS using VPH tracking.

In the measurement procedure, DCRM processes image $g(m,n)$ using Eq. (10) to obtain the intensity centre of the Airy disk in real time and automatically track the center position $P(x,y)$ of the Airy disk. It makes the PH centers coincident with the centre of Airy disk to eliminate the effect of PH lateral offset on position precision at confocal point and simplify the adjustment of the test lens R.

4. Determination of DCRMS key parameters and their effects

4.1 VPH size

As pinhole size decreases, the system sensitive increases while the energy received by the detector decreases. Hence, in a high system sensitive area, a larger pinhole should be selected to ensure enough energy passes through the pinhole. Analysis and calculation indicate that the pinhole size must satisfy Eq. (11), and an optimum pinhole should be in the range of 3–10μm in diameter [10,11].

$$d \leq \frac{2.5\lambda}{\pi \sin \alpha} \tag{11}$$

where d is the pinhole diameter, λ, the optical wavelength, $\sin\alpha$, the numerical aperture of L_2.

If the MO magnification is N, the pixels corresponding to the VPH diameter satisfies

$$d_{VPH} = \frac{N \cdot d}{p} \leq \frac{2.5N\lambda}{\pi p \sin \alpha} \tag{12}$$

where p is the pixel size of CCD.

4.2 VPH offset

As shown in Fig. 7, it is difficult for the offset of the two VPH to be equal in the amount under the adjustment of DCRM light-path. Assuming the offset of the two detectors are $M + \delta$ and $-M$ while their corresponding normalized offset are $u_M + u_\delta$ and u_M, and the offset of zeros O_A and O_B from focuses A and B are Δz_A and Δz_B, respectively, under the measurement while their normalized value are u_A and u_B.
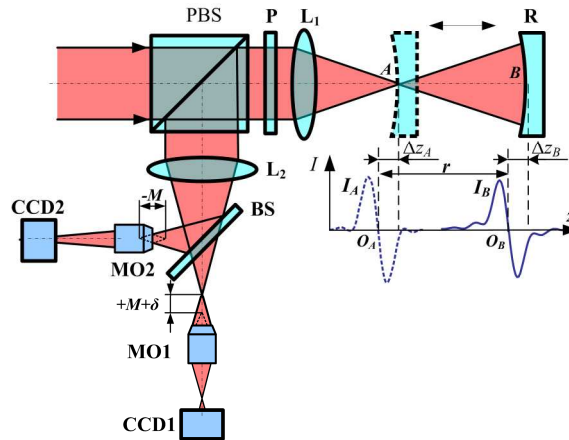

Fig. 7. Light-path principle with different offset of two detectors.

When L_1 and L_2 are the same in apertures, $p_C(\rho,\theta) = 1$, $p_1(\rho,\theta) = 1$, $p_2(\rho,\theta) = 1$ and the effect of figure error Φ is neglected, the axial responses at points O_A and O_B obtained using Eq. (3) and Eq. (4) satisfy

$$I_A(0,0,u_A,u_M) = \left[\frac{\sin\left((2u_A+u_\delta+u_M)/4\right)}{(2u_A+u_\delta+u_M)/4}\right]^2 - \left[\frac{\sin\left((2u_A-u_M)/4\right)}{(2u_A-u_M)/4}\right]^2 = 0 . \quad (13)$$

$$I_B(0,0,u_B,u_M,\Phi) = \left[\frac{\sin\left(2u_B+u_\delta+u_M\right)/4}{(2u_B+u_\delta+u_M)/4}\right]^2 - \left[\frac{\sin\left(2u_B-u_M\right)/4}{(2u_B-u_M)/4}\right]^2 = 0 . \quad (14)$$

From Eq. (13) and Eq. (14),

$$u_A = u_B = -\frac{u_\delta}{4} . \quad (15)$$

It can be seen from Eqs. (2) and (15) that the offset Δz_A and Δz_B of points O_A and O_B are equal, the radius measurement error caused by the VPH axial offset δ is

$$\Delta r_\delta = \Delta z_A - \Delta z_B = 0 . \quad (16)$$

It is obvious that in the DCRMS light-path adjustment, Δz_A and Δz_B caused by the offset of the detectors are the same in the size and direction so that they can counteract each other. And so, the adjustment difficulty of the detectors reduces greatly in DCRMS because the measurement error caused by δ is small.

4.3 Illumination collimation system

As shown in Fig. 8, it is difficult in the DCRMS light-path adjustment for the illumination collimation system to ensure the pinhole and the focus of collimation lens L_C in coincidence. This changes the defocused pupil function $p_C(\rho,\theta)$ of collimating lens L_C so that the curves $I_A(0,0,u,u_M)$ and $I_B(0,0,u,u_M,\Phi)$ are translated along the axial direction.

Assuming the PH offset is Δz_C while its corresponding normalized offset is u_C, and the offset of zeros O_A and O_B from focuses A and B are respectively Δz_A and Δz_B in the measurement while their normalized value are u_A and u_B. Then defocused pupil function $p_C(\rho,\theta)$ of the collimating lens L_C satisfies

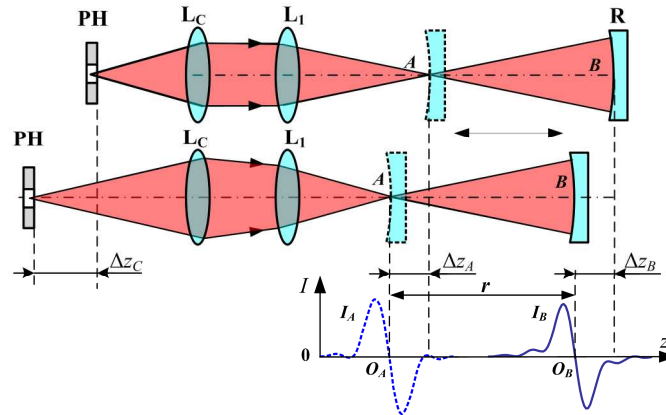$$p_C(\rho,\theta) = e^{j\rho^2(u_C/2)} . \quad (17)$$

Fig. 8. Effect of beam parallel of illumination collimating system.

Substituting Eq. (17) for Eqs. (1) and (4), when L_1 and L_2 are the same in apertures and the figure precision of the test lens is very high, the axial responses at points O_A and O_B obtained satisfy

$$I_A(0,0,u_A,u_M) = \left[\frac{\sin\left((2u_A+u_M+u_C)/4\right)}{(2u_A+u_M+u_C)/4}\right]^2 - \left[\frac{\sin\left((2u_A-u_M+u_C)/4\right)}{(2u_A-u_M+u_C)/4}\right]^2 = 0 \quad (18)$$

$$I_B(0,0,u_B,u_M,\Phi) = \left[\frac{\sin\left((2u_B+u_M+u_C)/4\right)}{((2u_B+u_M)+u_C)/4}\right]^2 - \left[\frac{\sin((2u_B-u_M+u_C)/4)}{(2u_B-u_M+u_C)/4}\right]^2 = 0 \quad (19)$$

From Eqs. (18) and (19),

$$u_A = u_B = -\frac{u_C}{2} \quad . \tag{20}$$

It can be seen from Eq. (2) and Eq. (20) that when the offset Δz_A and Δz_B of points O_A and O_B are equal, they can counteract each other. The radius measurement error caused by Δz_C is

$$\Delta r_C = \Delta z_A - \Delta z_B = 0 . \tag{21}$$

Hence, it greatly reduces the adjustment difficulty of DCRMS detectors because the measurement error caused by Δz_C is very small.

4.4 Nonlinear calibration of CCD detectors

The zero point is obtained through the differential subtraction of the normalized VPH data, so the difference of two CCDs in intensity response has little effect on the position of the zero point.

However, the nonlinearity of the intensity response has an effect on the determination of the zero point. Due to the discreteness of data in the measurement, the zero point can hardly be captured exactly, so the CCD nonlinearity must be calibrated and a linear curve can be fitted by the data near the zero point. And the calibration setup on CCD nonlinearity is shown in Fig. 9.
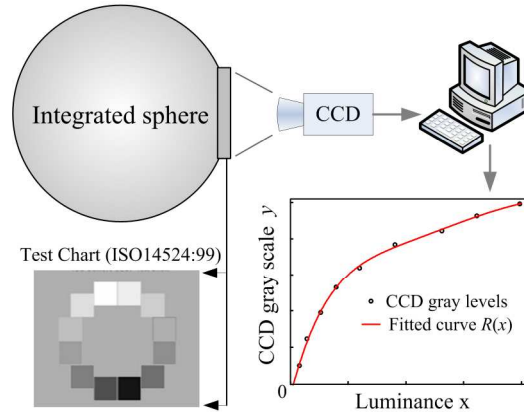

Fig. 9. Nonlinear calibration system of CCD intensity response.

The test chart in accordance with ISO14524:99 are placed at the outlet of the integrating sphere, and a set of grey values are shown in Table 1.

Table 1. Nonlinear calibration on CCD response

Normalized luminance	Normalized grey value of CCD	Normalized luminance	Normalized grey value of CCD
0.001	0.000	0.200	0.535
0.005	0.000	0.302	0.646
0.017	0.000	0.457	0.774
0.041	0.103	0.661	0.850
0.072	0.249	0.813	0.935
0.132	0.393	1.000	1.000

A set of grey data shown in Table 1 is obtained from the test chart using MTV-2821 CCD being calibrated. And the nonlinear calibration function $R^{-1}(y)$ shown in Fig. 10 are obtained through third-order polynomial fitting to the grey data, where x is the normalized luminance of the test chart and y is the normalized grey value of CCD output.
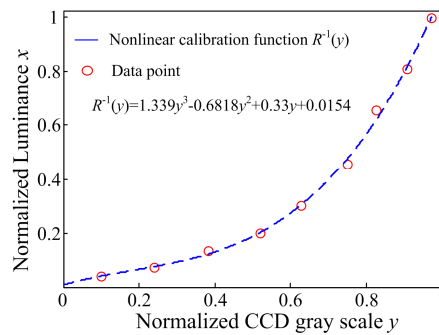

Fig. 10. Nonlinear calibration of CCD response curve.

The nonlinear calibration on the image $g(m,n)$ coming from CCD is made using $R^{-1}(y)$ in DCRMS and the response curves before and after calibration are shown in Fig. 11.
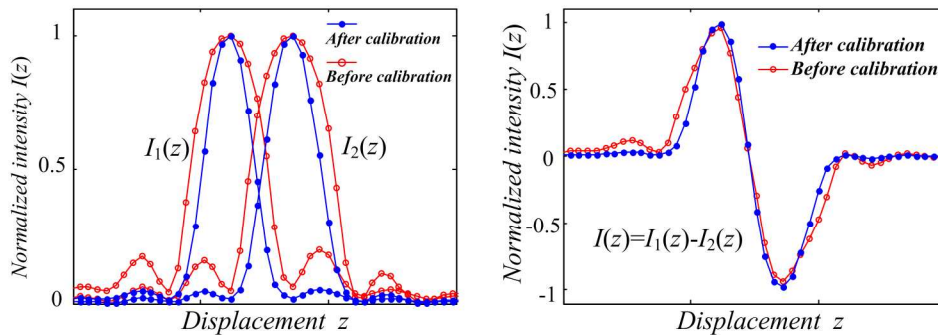

Fig. 11. Intensity response curves before and after calibration on CCD. a) Intensity response curves of two CCD b) DCS intensity curve.

It can be seen from Fig. 11 that the VPH response curve $I(z)$ is more coincident with the theory in shape after the calibration, its side lobe is suppressed obviously, its linearity is improved and its half width at half of a maximum is diminished.

4.5 Adjustment and correction of axial alignment errors

As shown in Fig. 12, the measurement axis d of a distance measurement interferometer (DMI), the motion axis of translation stages m and radius axis of lens measured t should be

coincident, whereas the angles between them always exist in practice. The angle between axes t and m is β and the angle between axes m and d is γ, the ROC measurement error is [3]

$$\sigma_{axial} = r(1 - \cos\beta \cdot \cos\gamma) . \qquad (22)$$

It can be seen from Eq. (22) that β and γ should be diminished to reduce the ROC measurement error σ_{axial}.

The angle γ is diminished through the careful alignment of DMI measurement axis d and motion axis of translation stage m and it is adjusted only at the time of establishing the system. And the correction of angle β is essential because it is produced by the placement of the test lens and should be adjusted for each test lens.

The adjustment of angle β in DCRMS is shown in Fig. 12, the center coordinate of the spot $p_A(x,y)$ is obtained using VPH when the test lens is translated to the cat's-eye position A, then the center coordinate of the spot $p_B(x,y)$ is obtained using VPH when the test lens is translated to the confocal position B, and thereby obtaining the lateral displacement ε of the spot centre.
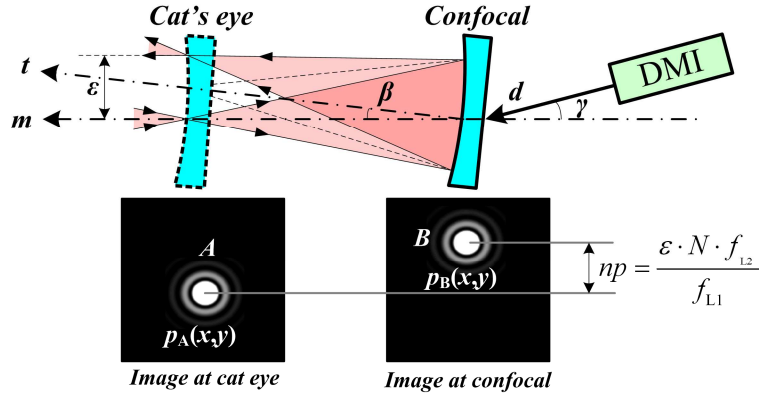

Fig. 12. Adjustment of angle β between optical axis t of the lens and motion axis m.

Angle β is obtained using the following equations, and

$$\tan\beta \approx \frac{\varepsilon}{2r_{DMI}} \qquad (23)$$

$$\varepsilon = \frac{n \cdot p \cdot f_{L1}}{N \cdot f_{L2}} \qquad (24)$$

where n is the pixel number corresponding to the lateral displacement of spot center from position A to position B, f_{L1} is the focal length of standard focusing lens L_1 and f_{L2} is the focal length of collecting lens L_2.

In the practical measurement, ROC measurement error caused by angle β can be corrected using Eq. (25).

$$r = \frac{r_{DMI}}{\cos\beta} = \frac{r_{DMI}}{\cos(\arc(\tan\beta))} \approx r_{DMI} / \cos(\frac{\varepsilon}{2r_{DMI}}) = r_{DMI} / \cos(\frac{n \times p \times f_{L1}}{2N \times f_{L2} \times r_{DMI}}) \quad (25)$$

where r_{DMI} is the radius measured by DMI.

The ROC measurement error σ_{axial} and the adjustment difficulty of the test lens reduce greatly because it caused by angle β can be corrected.

5. Measurement errors

The main errors having effects on ROC measurement are the distance measurement error of laser interferometer, position errors at cat's-eye position A and confocal position B, wave-front aberrations of sphere measured and axial alignment errors, and so on [3,14,15].

5.1 Distance measurement error σ_L

The distance *AB* between cat's-eye position A and confocal position B can be obtained by DMI, and its measurement precision is highly dependent on the deadpath error [8,9]. For the distance measurement, the variation of atmosphere in the laboratory is compensated by monitoring the temperature, pressure, and humidity real-timely. The measurement errors consist of: 1) σ_{Pa} for the barometer (pa), 2) σ_K for the thermometer (°C), and 3) σ_H for the hygrometer (% relative humidity).The distance measurement error satisfies:

$$\sigma_L = \sigma_{nair} \sqrt{\left(L_{deadpath}^2 + r^2\right)}$$
$$\approx \sqrt{\left(L_{deadpath}^2 + r^2\right)} \cdot \sqrt{\left(2.68 \times 10^{-9} \sigma_{Pa}\right)^2 + \left(-9.27 \times 10^{-7} \sigma_K\right)^2 + \left(-1 \times 10^{-8} \sigma_H\right)^2} \quad (26)$$

where σ_{nair} is the refraction index error of air, $L_{deadpath}$ is the difference between the DMI measurement and reference path lengths.

5.2 Null error σ_z

When the figure precision of the test sphere is high, the figure error is negligible, and the identification sensitivity $S(0,0,0, u_M)$ is calculated by differentiating Eq. (3) on u.

$$S(0,0,0,u_M) = \frac{\partial I_A(0,0,u,u_M)}{\partial u}\bigg|_{u=0} = 2 \cdot \text{sinc}(\frac{u_M}{4\pi}) \cdot \left[\frac{\left(\frac{u_M}{4}\right) \cdot \cos\left(\frac{u_M}{4}\right) - \sin\left(\frac{u_M}{4}\right)}{\left(\frac{u_M}{4}\right)^2}\right]. \quad (27)$$

The sensitivity of the differential intensity curve is the largest and $S_{max} = -0.54$ at the zero point when $u_M = 5.21$ [10,11]. And the DCS null error δz and the relative aperture D/f' of confocal objective satisfy Eq. (28).

$$\sigma_z = \frac{\delta I_A(0,0,u,u_M)}{-0.54} \cdot \frac{2\lambda}{\pi(D/f')^2} = -\frac{1.18\lambda}{SNR \cdot (D/f')^2} \quad (28)$$

where $\delta I_A(0,0,u,u_M)$ is the random noise of normalized differential signal caused by CCD of VPH, *SNR* is the signal noise ratio of VPH and their relation is $SNR = 1/\delta I_A(0,u,u_M)$. It can be seen from Eq. (28) that the measurement precision increases as D/f' increases.

5.3 Axial alignment errors σ_{axial}

The residual error $\delta\beta$ obtained using Eq. (25) after the adjustment and correction is

$$\delta\beta = \arctan\left(\frac{\delta\varepsilon}{2r}\right) \approx \frac{\delta\varepsilon}{2r} = \frac{\delta n \cdot p \cdot f_{L1}}{2N \cdot f_{L2} \cdot r} \quad (29)$$

where *p* is the pixel size of CCD.

The position precision of the spot center is $\delta n = 0.1$ through the sub-pixel subdivision. When $N = 10$, $p = 8\mu m$, $f_{L1} = 9mm$ and $f_{L2} = 160mm$, the residual error obtained using Eq. (29) is $\delta\beta = 0.000023mrad$ with radius $r = 100mm$. Hence, the measurement error of *r* caused by $\delta\beta$ is negligible.

The angle γ between DMI and motion stage can be less than 0.5 mrad through the careful adjustment [3].

Radius measurement error σ_{axial} caused by the misalignment of the DMI measurement axis d, the motion axis of translation stages m and radius axis of lens measured t is

$$\sigma_{axial} = r(1 - \cos\beta \cdot \cos\gamma) \approx r(1 - \cos\gamma) = r(1 - \cos 0.0005) \approx 1.24 \times 10^{-7} r \quad . \quad (30)$$

5.4 Figure error σ_{figure}

The analyses indicate that the effect of figure error on identification precision at DCRMS confocal position B is negligible for the test sphere with high precision.

The cat's-eye point does not correspond to the best-fit sphere and it lies in a small area of the test lens surface, so that a figure error at wavelength level is introduced. And the error σ_{figure} can be corrected by the figure of the test sphere obtained by phase shift interferometer, and the figure error after the correction satisfies [3]:

$$\sigma_{figure} \approx 0.1 \cdot PV . \quad (31)$$

5.5 Synthesis error

Considering the effect of the aforementioned several errors on the measurement results, the total measurement error σ_r is

$$\sigma_r \approx \sqrt{\sigma_L^2 + 2 \cdot \sigma_z^2 + \sigma_{axial}^2 + \sigma_{figure}^2} \quad (32)$$

When the parameters of the test lens are $r = 100$mm, $D = 20$mm and $PV = 0.1\lambda$, the magnification of objective used for VPH is $N = 10$, the CCD pixel size is $p = 8\mu$m and signal noise ratio is $SNR = 150:1$, the errors obtained using Eqs. (26)~(31) are $\sigma_L \approx 0.1\mu$m, $\sigma_z \approx 0.1\mu$m, $\sigma_{axial} \approx 0.01\mu$m and $\sigma_{figure} \approx 0.01\mu$m, respectively.

The system measurement error obtained using Eq. (32) is

$$\sigma_r \approx \sqrt{\sigma_L^2 + 2 \cdot \sigma_z^2 + \sigma_{axial}^2 + \sigma_{figure}^2} = \sqrt{(0.1)^2 + 2 \times (0.1)^2 + (0.01)^2 + (0.01)^2} \, \mu m \approx 0.17 \mu m . \quad (33)$$

Its relative error is

$$\delta_r \approx \left| \frac{\sigma_r}{r} \right| \times 100\% \approx \left| \frac{0.17}{100 \times 1000} \right| \times 100\% = 0.00017\% \approx 2\text{ppm} . \quad (34)$$

The system relative measurement error can be better than 5ppm with the consideration of environment and some negligible errors.

6. Experiments

6.1 Experiment setup

The experimental setup shown in Fig. 13 is established based on Fig. 6 to verify the validity of DCRM proposed.
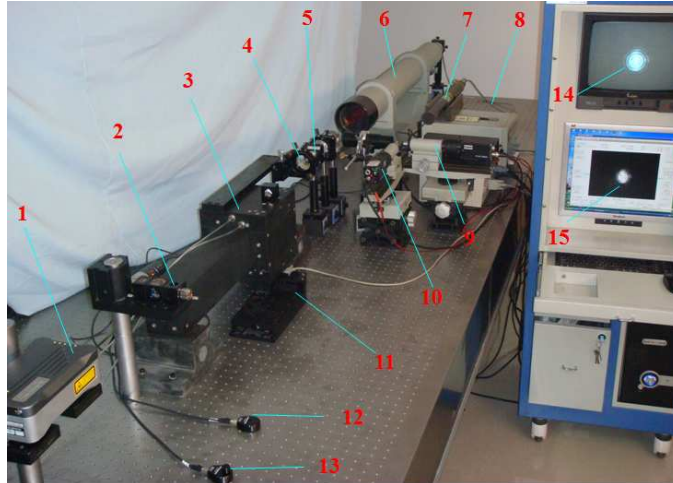
Fig. 13. Experimental setup. (1) X80 laser interferometer produced by RENISHAW, (2) Interferometry measurement prisms, (3) Air bearing slider, (4) Test lens, (5) Standard focusing lens, (6) Collimator, (7) He-Ne laser, (8) Single-mode fiber, (9) CCD confocal detection system 1, (10) CCD confocal detection system 2, (11) Drive motor, (12) Material sensor, (13) Air sensor, (14) Monitor, (15) Image capture and soft process system.

The environmental conditions in the measurement laboratory are: pressure = (102540 ± 60) Pa, temperature = (20 ± 0.2) °C and relative humidity = (40 ± 4) %. In the experiment, the objective lens of M-20X, N.A. = 0.40 and f_{L1} = 9.0mm produced by NEWPORT is used as standard focusing L_1, the focal length of collecting lens L_2 is f_{L2} = 160mm, the CCD used is MTV-2821, the magnification of VPH microscope objective is $N = 10 \times$, DMI used is X80 laser interferometer produced by RENISHAW, and motion rail used is high-precision air bearing slider of 300mm in range and 0.1μm in straightness. The test sphere used is concave, its diameter is 42mm and the ROC of its front surface is $r = -36.697$mm obtained by the traveling microscope with the uncertainty of 0.002mm [2].

6.2 Experiment

As shown in Fig. 6, when the test lens R is moved along the optical axis under the measurement, DCRMS uses the null O_A of DCS intensity curve I_A to precisely determine the cat's-eye position A. The null O_A of DCS intensity curve I_A as shown in Fig. 14 corresponds to the cat's-eye position A, and the position coordinate corresponding to O_A is 36.69542mm. Then, the pixel coordinate of the spot centre obtained by VPH $p_A(x,y)$ is (376.6, 309.1).
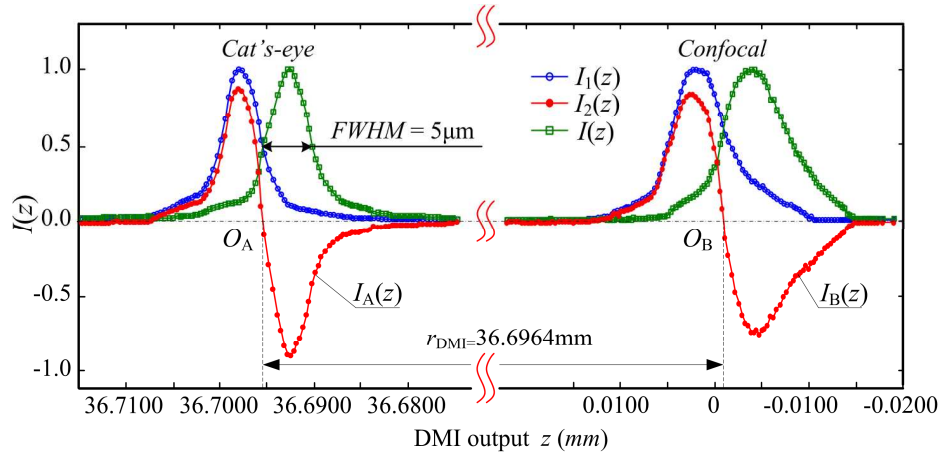
Fig. 14. Radius measurement curves.

Similarly, when the test lens R is moved near the confocal position B under the measurement, DCRMS uses the null O_B of DCS curve I_B to precisely determine the confocal position B, and the position coordinate corresponding to O_B is -0.00093mm. Then, the pixel coordinate of the spot centre obtained by VPH $p_B(x,y)$ is (383.7, 280.5).

So, the distance between O_A and O_B is $r_{DMI} \approx 36.6964$mm. As shown in Fig. 12, the pixel distance between $p_A(x,y)$ and $p_B(x,y)$ is

$$n = \sqrt{(376.6 - 383.7)^2 + (309.1 - 280.5)^2} \approx 29.5 . \tag{35}$$

Then, ROC of the test lens obtained using Eq. (25) is

$$r = r_{DMI} / \cos(\frac{n \cdot p}{2N \cdot r_{DMI}}) = (-0.00093 - 36.69542) / \cos(\frac{29.5 \times 0.008}{2 \times 10 \times (-0.00093 - 36.69542)}) \tag{36}$$

$$\approx -36.6964 mm$$

The figure error of the test lens obtained by Zygo interferometer is shown in Fig. 15, PV = 0.208λ and the radius deviation caused by the figure error is 0.037λ. So, the radius obtained after error correction is

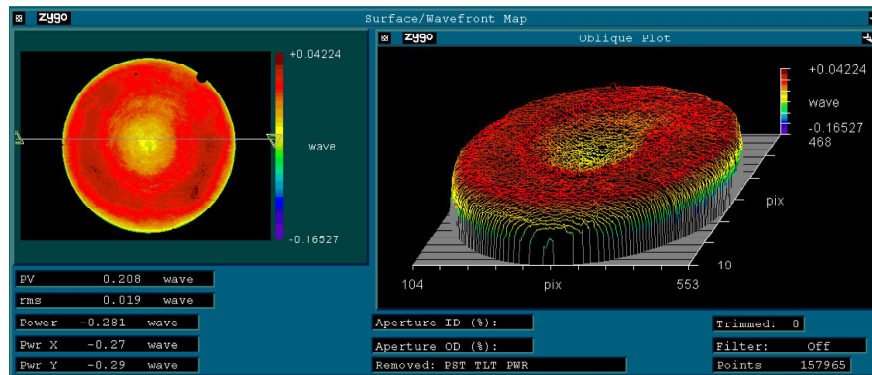$$r = -36.6964 + 0.037 \times 0.0006328 \approx -36.6964 mm . \tag{37}$$

Fig. 15. Figure errors of the test lens.

The air sensor of X80 is used to monitor the temperature, pressure and humidity real-timely for compensating the laboratory environment. The errors are: 1) σ_{Pa} = 50pa for the

barometer, 2) $\sigma_K = 0.1°C$ for the thermometer, and 3) $\sigma_H = 3\%$ for the hygrometer. The DCRM deadpath is $L_{deadpath} = 0.6m$. The distance measurement error obtained by Eq. (26) is

$$\begin{aligned}\sigma_L &= \sqrt{\left(L_{deadpath}^2 + r^2\right)} \cdot \sqrt{\left(2.68 \times 10^{-9} \sigma_{Pa}\right)^2 + \left(-9.27 \times 10^{-7} \sigma_K\right)^2 + \left(-1 \times 10^{-8} \sigma_H\right)^2} \\ &= \sqrt{\left(600^2 + 36.6964^2\right)} \times \sqrt{\left(2.68 \times 10^{-9} \times 50\right)^2 + \left(-9.27 \times 10^{-7} \times 0.1\right)^2 + \left(-1 \times 10^{-8} \times 3\right)^2} \approx 0.0001mm\end{aligned} \tag{38}$$

σ_{axial} caused by the misalignment obtained by Eq. (30) is

$$\sigma_{axial} = 1.24 \times 10^{-7} r = 1.24 \times 10^{-7} \times (-36.6964) = -5nm . \tag{39}$$

The relative aperture of the objective lens M-20X is 0.87, the CCD pixel size is $p = 8\mu m$ and signal noise ratio is $SNR = 150{:}1$, the null error obtained using Eq. (28) is

$$\sigma_z = -\frac{1.18\lambda}{SNR \cdot (D/f')^2} = -\frac{1.18 \times 0.6328}{150 \times 0.87^2} = -0.007\mu m . \tag{40}$$

The figure error of the test lens is PV = 0.208λ, and the radius error caused by the figure error obtained using Eq. (28) is

$$\sigma_{figure} \approx 0.1 \cdot PV = 0.1 \times 0.208 \times 0.6328 = 0.013\mu m . \tag{41}$$

The whole measurement error obtained using Eq. (32) is

$$\begin{aligned}\sigma_r &\approx \sqrt{\sigma_L^2 + 2 \cdot \sigma_z^2 + \sigma_{axial}^2 + \sigma_{figure}^2} \\ &= \sqrt{(0.1)^2 + 2 \times (-0.007)^2 + (-0.005)^2 + (0.013)^2}\,\mu m \approx 0.10\mu m\end{aligned} \tag{42}$$

Its relative error is

$$\delta_r \approx \left|\frac{\sigma_r}{r}\right| \times 100\% \approx \left|\frac{0.10}{-36.6964 \times 1000}\right| \times 100\% = 0.00027\% \approx 3\text{ppm} . \tag{43}$$

7. Conclusions

The differential confocal radius measurement proposed uses the zero point of DCS axial intensity response to precisely identify the cat's-eye position and confocal position as to achieve the high-precision ROC measurement. The preliminary experiments indicate that the relative error of the differential confocal radius measurement proposed is better than 5ppm, and the approach proposed

1) improves obviously the identification precision at cat's-eye position and confocal position because its linearity and sensitivity are the best at the zero of DCS intensity response curve.

2) has a strong environmental anti-interference capability because it uses the DCS intensity response curve obtained through differential subtraction as focusing criterion.

3) is easily combined with pupil filtering to suppress the focal-depth of standard lens, and consequently improves the identification sensitivity.

The approach proposed has the potential to be a high-accuracy, compact, simple, and low-cost detector for implementations of the radius bench method.

Acknowledgment